

# Dual-acceptor alloy model delivers high detection performance of organic NIR detectors for real-time arterial pulse monitoring

Xiaoyang Du, Zeyu He, Luye Cao, Xin Yu, Silu Tao\*

School of Optoelectronic Science and Engineering, University of Electronic Science and Technology of China, No.2006, Xiyuan Ave, West Hi-Tech Zone, Chengdu 610054, China

**Abstract.** Near-infrared organic photodetectors (NIR-OPDs) have significant potential in the fields of human sign monitoring, industrial defect detection, and military. We propose a method to construct high-performance NIR-OPDs by introducing narrow-band acceptor materials with very similar structures in bulk heterojunctions (BHJs) so that they form an alloy model during the film formation process, which in turn promotes the generation and dissociation of photogenerated excitons to achieve high-performance NIR detectors. Here, we choose the narrow-band materials IEICO-4F and IEICO-4Cl as dual-acceptors and PTB7-Th as the donor to construct NIR-OPDs. Benefiting from the alloy model formation, the dark current of the device is significantly suppressed compared with the binary control, while the photocurrent of the device is enhanced. The optimized NIR-OPD achieved a detectivity of more than  $2.6 \times 10^{12}$  Jones at -0.1V bias. With the optimized device performance, we can clearly monitor the human arterial pulse information, and the phases of the cardiac cycle of the heart can be accurately identified. This work demonstrates a new method for constructing high-performance NIR-OPDs and shows great potential for contactless human arterial pulse monitoring.

## 1 Introduction

Organic semiconductor, which has the advantages of flexible, lightweight, adjustable band gap, solution processable, showing great potential for future applications in wearable devices.[1-6] Among the many organic semiconductor devices, near-infrared organic photodetectors (NIR-OPDs) are capable of converting NIR optical signals into electrical signals, and have significant potential for development in the fields of communications, military, and security.[7-11] Benefiting from the continuous development of novel organic semiconductor materials, OPDs have achieved comparable performance to inorganic photodetectors in the visible light region. However, the dark current density ( $J_D$ ) of NIR-OPDs is usually large due to the intrinsic properties of narrow-band organic semiconductor materials, which leads to unsatisfactory detection performance of NIR-OPDs.[7, 12-14]

To solve this problem, we propose a new strategy to construct NIR detectors using a narrow-band acceptor alloy model, which not only provides a more efficient charge transfer channel, but also improves the microscopic morphology of the bulk heterojunction to reduce the dark current of the device, thus achieving high detection performance of NIR-OPD. In this work, the narrow-band acceptor 2,2'-((2Z,2'Z)-(((4,4,9,9-tetrakis(4-hexylphenyl)-4,9-dihydro-sindaceno[1,2-b:5,6-b']-dithiophene-2,7-diyl)bis(4-((2-ethylhexyl)oxy)thiophene-5,2-diyl)bis(methanylylidene))bis(5,6-difluoro-3-oxo-2,3-dihydro-1H-indene-2,1-diylidene))dimalono-

nitrile (IEICO-4F) and 2,2'-((2Z,2'Z)-(((4,4,9-tris(4-hexylphenyl)-9-(4-pentylphenyl)-4,9-dihydro-s-indaceno[1,2-b:5,6-bdithiophene-2,7-diyl)bis(4-((2-ethylhexyl)oxy)thiophene-5,2-diyl)bis(methanylylidene))bis(5,6-dichloro-3-oxo-2,3-dihydro-1H-indene-2,1-diylidene))dimalononitrile (IEICO-4Cl) were used to form an alloy model, they can provide NIR absorption over 1000 nm.[15-17] Poly(4,8-bis(5-(2-ethylhexyl)thiophen-2-yl)benzo[1,2-b;4,5-b0]dithiophene-2,6-diylalt-(4-(2-ethylhexyl)-3-fluorothieno[3,4-b]thiophene)-2-carboxylate-2,6-diyl (PTB7-Th) was chose as the donor for its high hole mobility and matched charge transport energy level orbitals.[18, 19] The absorption spectrum of the ternary hybrid film covered the full spectral range of 300-1100nm, ensuring an efficient NIR response. Due to the introduction of alloy model acceptors, ternary heterojunctions exhibit more efficient photogenerated exciton generation, exciton dissociation and carrier transport. It is noteworthy that the alloy-model based film presented smaller roughness and more uniform material distribution compared to the binary control, which is one of the reasons for the reduced dark current of the devices. As results, a high responsivity of 0.37 A/W and maximum detectivity ( $D^*$ ) of  $2.6 \times 10^{12}$  Jones at -0.1V bias have been realized. Based on above optimizations, we have realized highly accurate real-time human arterial pulse monitoring by using our NIR-OPD, from which the phases of the heart's cardiac cycle and information such as heart rate can be clearly identified.

\* Corresponding author: [silutao@uestc.edu.cn](mailto:silutao@uestc.edu.cn).

## 2 Results and discussion

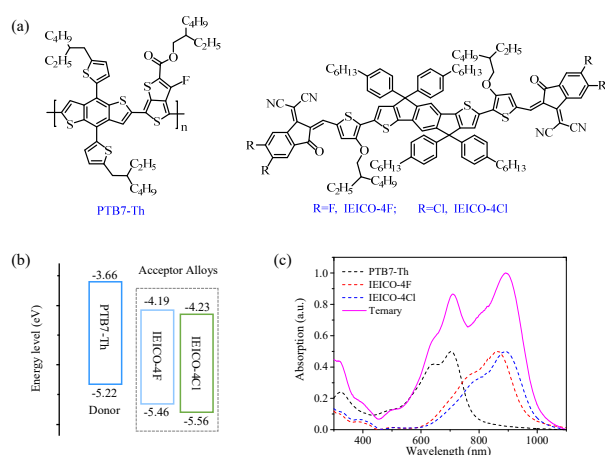


**Fig. 1.** (a) Material structures of PTB7-Th, IEICO-4F and IEICO-4Cl; (b) energy level of PTB7-Th, IEICO-4F and IEICO-4Cl, where IEICO-4F and IEICO-4Cl can form alloys; (c) normalized absorption structure of PTB7-Th, IEICO-4F, IEICO-4Cl and PTB7-Th: IEICO-4F: IEICO-4Cl films.

The molecular structures of the acceptor materials used to construct the alloy model and the matching donor material are shown in Fig. 1. (a). It is evident that IEICO-4F and IEICO-4Cl have very similar molecular structures, which can ensure their eutectic formation during the film formation process and thus form the alloy model. PTB7-Th was chosen as the donor for its high hole mobility and appropriate energy level as shown in Fig. 1. (b), which guarantees efficient exciton dissociation and charge transport. IEICO-4F exhibited a highest occupied molecular orbital (HOMO) energy level of -5.46 eV and a lowest unoccupied molecular orbital (LUMO) energy level of -4.19 eV, while IEICO-4Cl showed a lower LUMO of -4.23 eV and HOMO of -5.56 eV. Fig. 1. (c) shows the absorption spectra of monomeric and hybrid films. The absorption spectrum of PTB7-Th covers the range of 300-800 nm and is complementary to the absorption spectra of the acceptors. Compared with IEICO-4F, IEICO-4Cl exhibits a red-shifted absorption spectrum, which gives the detector a broader detection range. As a result, the film composed of PTB7-Th, IEICO-4F and IEICO-4Cl exhibits a wide absorption range of 300-1100 nm, especially in the near-infrared region, which is the key to the construction of NIR-OPD.

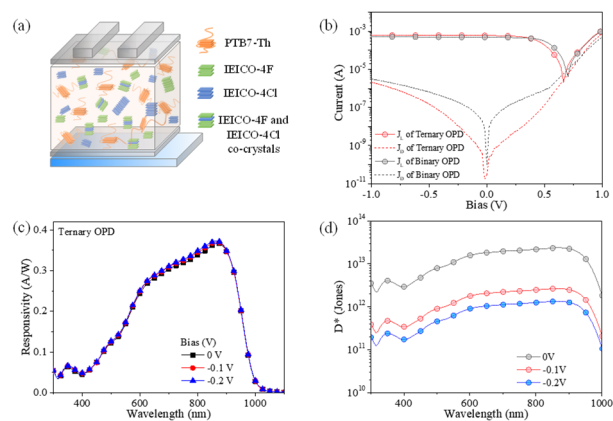


**Fig. 2.** (a) Device structure and schematic diagram of material distribution within the photosensitive layer of the optimized NIR-OPD; (2) the current density in the dark and under 980 nm light irradiation of the binary and ternary NIR-OPDs; (3) the responsivity of optimized NIR-OPD at 0 V, -0.1 V and -0.2 V bias; (4) the D\* of optimized NIR-OPD at 0 V, -0.1 V and -0.2 V bias.

The device structure and schematic diagram of material distribution within the photosensitive layer of the optimized NIR-OPD are shown in Fig. 2. (d), the functional layers from bottom to top are ITO/ ZnO/ photosensitive layer/ MoO<sub>3</sub>/ Ag. In the schematic diagram, orange represents the polymer feeder, green and blue stands for IEICO-4F and IEICO-4Cl respectively. A portion of IEICO-4F and IEICO-4Cl would form eutectic and all materials would be uniformly distributed in the photosensitive layer. Subsequently, we tested the I-V characteristics of the optimized NIR-OPD and the control in the dark and under 980 nm NIR light illumination. As shown in Fig. 2. (b), the photoresponse of the ternary OPD based on the dual-acceptor alloy model was significantly higher than that of the corresponding binary control under the same power of 980 nm NIR light irradiation. The enhancement of photocurrent is attributed to the formation of a double-acceptor alloy model to enhance the exciton generation efficiency and dissociation efficiency on the one hand, and to the construction of stepped charge transport channels to improve the carrier transport and extraction efficiency on the other hand. In addition, the dark currents of the ternary device are also significantly lower than that of the comparison devices, which may be explained by the introduction of the third acceptor to improve the microscopic morphology of the co-blended films. The responsivity curve calculated from the EQE is shown in Fig. 2. (c) and is calculated as:  $R = EQE \times q \lambda / hc$ . [20] Here q is elemental charge,  $\lambda$  is incident NIR light wavelength, h is Planck's constant and c is velocity of light. As shown in Fig. 2. (c), as the bias voltage increases, the response of the device increases. The optimized NIR-OPD achieved a maximum responsivity of 0.37 A/W at -0.2 V bias. In addition to the responsivity of the device, the detectivity (D\*) is also a key parameter to measure whether the detector can meet the requirements of practical applications. Typically, the noise of the OPD is dominated by the shot noise of the dark current under reverse bias. Therefore, D\* can be described by the equation  $D^* = R / (2qJ_D)^{1/2}$ , [21] where R is above calculated

responsivity,  $q$  is elemental charge and  $J_D$  is dark current density. Fig. 2. (d) reveals the wavelength-dependent  $D^*$  curves of the optimized NIR-OPD under different bias. The optimized NIR-OPD achieved a maximum  $D^*$  of  $2.36 \times 10^{13}$  Jones without an applied bias, and the  $D^*$  of the device were  $2.64 \times 10^{12}$  Jones and  $1.34 \times 10^{12}$  Jones when the applied bias was increased to 0.1 V and 0.2 V, respectively. Therefore, we can conclude that  $D^*$  tends to decrease with increasing bias voltage, which indicates that the dark current of the NIR-OPD directly determines the upper limit of  $D^*$ .

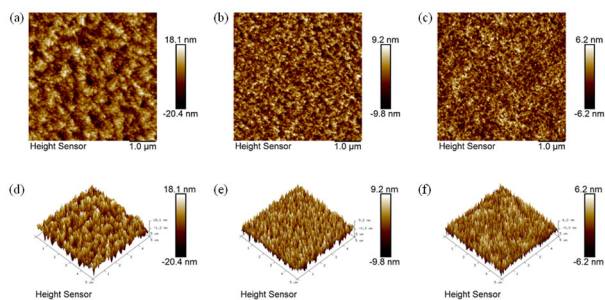


**Fig. 3.** 2D AFM images of (a) PTB7-Th: ICIEO-4F, (b) PTB7-Th: ICIEO-4Cl and (c) PTB7-Th: ICIEO-4F: ICIEO-4Cl-based films; 3D AFM images of (d) PTB7-Th: ICIEO-4F, (e) PTB7-Th: ICIEO-4Cl and (f) PTB7-Th: ICIEO-4F: ICIEO-4Cl-based films.

The changes in the charge dynamics of the NIR-OPDs are closely related to the variations in the microscopic morphology of the photosensitive layers. We investigated the control and optimized films morphology using atomic force microscope (AFM) as shown in Fig. 3. From the 2D images (Fig. 3. (a)-(c)), the PTB7-Th: IEICO-4F and PTB7-Th: IEICO-4Cl based films exhibited a high root-mean-square (RMS) surface roughness of 5.58 nm and 2.77 nm, respectively. When IEICO-4F and IEICO-4Cl were mixed together to construct the alloy model ternary heterojunction, the RMS of the ternary film was reduced to 1.79 nm. Along with the reduced RMS, the ternary blend film also exhibited optimized material distribution and suppressed material aggregation phenomena. Fig. 3. (d)-(f) showed the 3D AFM images of the control and optimized films, it is quite evident that the fluctuations of the ternary film were weaker than the binary references, which is consistent with the pattern reflected by 2D AFM images. The AFM results suggest that the optimized NIR-OPD based on the alloy model has a more uniform material distribution and smoother functional layer contact surface, which is one of the reasons for the lower dark current of the device.

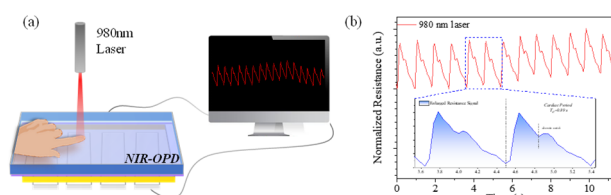


**Fig. 4.** (a) Diagram of finger arterial pulse test; (b) Normalized resistance signal curve of the finger artery pulse, the insert is enlarged resistance signal.

Based on the excellent detection performance of this optimized NIR-OPD, we further used it for human finger artery pulse monitoring, and the operation schematic is shown in Fig. 4. (a). Here, 980 nm laser is used as the detection source, the NIR light penetrates through the finger and is received by the NIR-OPD. As the heart pumps and contracts, the finger arteries expand causing a change in light flux, which in turn causes a change in the detection signal. Fig. 4. (b) shows the measured resistance signal of human finger artery, and the insert graph is enlarged resistance signal from the main curve. From the figure, it is obvious that each waveform is very similar and all show rich and detailed information about the arterial pulse: 1. We can accurately calculate the human being beats per minute (BPM) of the tested person as 69; 2. We can accurately identify the systolic and diastolic phases of the cardiac cycle, which in turn translates to a cardiac cycle of 0.89 s for the subject; 3. The demarcation point between ventricular systole and diastole, the so-called dicrotic notch, was well localized; 4. The P1-P5 processes of cardiac rapid ejection, slow ejection, ventricular systole and ventricular diastole can be clearly and readily recognized. This detailed cardiac cycle information is consistent with current commercially available piezoelectric pulse detection results, demonstrating the great potential of the optimized NIR-OPD for future non-contact arterial pulse monitoring in medical applications.

### 3 Conclusion

In summary, we propose a new strategy for constructing high-performance NIR-OPDs, that is, introducing a dual-acceptor material with similar molecular structure into the bulk heterojunction to form an alloy model, which can effectively enhance the optical response of the detector on the one hand, and improve the microscopic morphology of the photosensitive layer and thus effectively suppress the dark current of the device on the other hand. Therefore, the optimized NIR-OPD achieved a high  $D^*$  of more than  $2.6 \times 10^{12}$  Jones at -0.1V bias. Finally, based on the excellent detection performance of this optimized NIR-OPD, human finger artery pulse monitoring application using it was developed. In the monitored signal, heart rate, cardiac cycle and its phases can be accurately distinguished, which is comparable to commercially available piezoelectric pulse detection results. The NIR-OPD reported in this work shows great potential for non-contact real-time pulse monitoring in the future medical field.

### 4 Device Fabrication and Measurements

The device structure of NIR-OPD is ITO/ ZnO/ BHJ/ MoO<sub>3</sub>/ Ag. The ITO substrates were cleaned using detergent, deionized water, ethyl alcohol, acetone and ethyl alcohol for every 15 min, and then treated in ultraviolet ozone for 20 min. The ZnO precursor was prepared via mixing zinc acetate dihydrate (110 mg) and ethanolamine (31 mg) in 2-methoxyethanol solution (1 ml)

and stirred over a night. Then the precursor was spin-coated on ITO substrates with 5000 rpm for 30 s and then annealed at 200 °C for 30 min. For binary BHJs, PTB7-Th and IEICO-4F or IEICO-4Cl were mixed in CB: 2%CN solution with a ratio of 1:1.5 (w/w), the donor concentration is 8 mg/ml. Similarly, for ternary BHJ, PTB7-Th, IEICO-4F and IEICO-4Cl were also mixed in CB: 2%CN solution with a ratio of 1:1:0.5 (w/w), the donor concentration is 8 mg/ml. MoO<sub>3</sub> was deposited on photosensitive layer by vacuum vapor with a ratio of 0.1 Å/s, and then Ag was deposited with a ratio of 1 Å/s to form 100nm electrodes. The absorption spectra were measured by Hitachi U-3010 UV-VIS. The film morphology of BHJ and G-BHJ were studied via Atomic force microscope (AFM, Asylum Research AFM system (MFP-3D-BIO)). The photoresponse characteristics of OPDs were measured by a PDA semiconductor analyzer with probe station. External quantum efficiency (EQE) properties of detection unit were performed with a Keithley 2400 source meter instrument and a QEX10 Quantum Efficiency Measurement System.

## Acknowledgements

The work was supported by the National Natural Science Foundation of China (NSFC Grant Nos. 62075029, 52130304 and 62105055), The China Postdoctoral Science Foundation (2020TQ0058 and 2021M7006), the Fundamental Research Funds for the Central Universities (Program No. ZYGX2021J017).

## References

- [1] J. Zhang, W. Xu, P. Sheng, G. Zhao, D. Zhu, *Acc. Chem. Res.* **50**, 1654 (2017)
- [2] B. Zheng, L. Huo, *Sci. China: Chem.* **64**, 358 (2021)
- [3] Y. Qian, X. Zhang, L. Xie, D. Qi, B. K. Chandran, X. Chen, W. Huang, *Adv. Mater.* **28**, 9243 (2016)
- [4] A. D. Scaccabarozzi, A. Basu, F. Aniés, J. Liu, O. Zapata-Arteaga, R. Warren, Y. Firdaus, M. I. Nugraha, Y. Lin, M. Campoy-Quiles, N. Koch, C. Müller, L. Tsetseris, M. Heeney, T. D. Anthopoulos, *Chem. Rev.* **122**, 4420 (2022)
- [5] N. Sakai, R. Warren, F. Zhang, S. Nayak, J. Liu, S. V. Kesava, Y.-H. Lin, H. S. Biswal, X. Lin, C. Grovenor, T. Malinauskas, A. Basu, T. D. Anthopoulos, V. Getautis, A. Kahn, M. Riede, P. K. Nayak, H. J. Snaith, *Nat. Mater.* **20**, 1248 (2021)
- [6] C. Wang, H. Dong, L. Jiang, W. Hu, *Chem. Soc. Rev.* **47**, 422 (2018)
- [7] Z. Wu, Y. Zhai, H. Kim, J. D. Azoulay, T. N. Ng, *Acc. Chem. Res.* **51**, 3144 (2018)
- [8] J. H. Kim, A. Liess, M. Stolte, A.-M. Krause, V. Stepanenko, C. Zhong, D. Bialas, F. Spano, F. Würthner, *Adv. Mater.* **33**, 2100582 (2021)
- [9] M. Qin, Q. Li, Y. Guo, Y. Liu, *Semicond. Sci. Technol.* **35**, 114001 (2020)
- [10] J. Liu, M. Gao, J. Kim, Z. Zhou, D. S. Chung, H. Yin, L. Ye, *Mater. Today* **51**, 475 (2021)
- [11] J. Liu, J. Jiang, S. Wang, T. Li, X. Jing, Y. Liu, Y. Wang, H. Wen, M. Yao, X. Zhan, L. Shen, *Small* **17**, 2101316 (2021)
- [12] Y. Wei, H. Chen, T. Liu, S. Wang, Y. Jiang, Y. Song, J. Zhang, X. Zhang, G. Lu, F. Huang, Z. Wei, H. Huang, *Adv. Funct. Mater.* **31**, 2106326 (2021)
- [13] Z. Wu, W. Yao, A. E. London, J. D. Azoulay, T. N. Ng, *Acc. Chem. Res.* **28**, 1800391 (2018)
- [14] B. Park, J. Jung, D.-H. Lim, H. Lee, S. Park, M. Kyeong, S.-J. Ko, S. H. Eom, S.-H. Lee, C. Lee, S. C. Yoon, *Adv. Funct. Mater.* **32**, 2108026 (2022)
- [15] P. Jacoutot, A. D. Scaccabarozzi, T. Zhang, Z. Qiao, F. Aniés, M. Neophytou, H. Bristow, R. Kumar, M. Moser, A. D. Nega, A. Schiza, A. Dimitrakopoulou-Strauss, V. G. Gregoriou, T. D. Anthopoulos, M. Heeney, I. McCulloch, A. A. Bakulin, C. L. Chochos, N. Gasparini, *Small* **18**, 2200580 (2022)
- [16] M. H. Rahaman, J. Holland, M. A. Hossain, L. Duan, B. Hoex, P. Mota-Santiago, V. D. Mitchell, A. Uddin, J. A. Stride, *Sol. RRL* **6**, 2200184 (2022)
- [17] Y. Cui, C. Yang, H. Yao, J. Zhu, Y. Wang, G. Jia, F. Gao, J. Hou, *Adv. Mater.* **29**, 1703080 (2017)
- [18] Y. Zang, X. Gao, Q. Xin, J. Lin, J. Zhao, *Appl. Phys. A* **123**, 398 (2017)
- [19] D. Yang, F. C. Lhrer, V. Krstgens, A. Schreiber, S. Bernstorff, J. M. Buriak, P. Müller-Buschbaum, *ACS Energy Lett.* **4**, 464 (2019)
- [20] C. Li, H. Wang, F. Wang, T. Li, M. Xu, H. Wang, Z. Wang, X. Zhan, W. Hu, L. Shen, *Light: Sci. Appl.* **9**, 31 (2020)
- [21] J. Huang, J. Lee, J. Vollbrecht, V. V. Brus, A. L. Dixon, D. X. Cao, Z. Zhu, Z. Du, H. Wang, K. Cho, G. C. Bazan, T.-Q. Nguyen, *Adv. Mater.* **32**, 1906027 (2020)